

The sulfate-methane transition as a proxy for average methane hydrate saturation in marine sediments

G. Bhatnagar¹, W. G. Chapman¹, G. R. Dickens², B. Dugan², G. J. Hirasaki^{1*}

¹*Department of Chemical & Biomolecular Engineering, Rice University, Houston, Texas*

²*Department of Earth Science, Rice University, Houston, Texas*

* Corresponding author: gjh@rice.edu

Abstract.

We develop a relationship between the sulfate-methane transition (SMT) and average gas hydrate saturation (AGHS) for systems dominated by methane migration from deeper sources. The relationship is explained by a one-dimensional numerical model that simulates gas hydrate accumulation in marine sediments. Higher methane fluxes result in shallow SMT depths and high AGHS, while lower methane fluxes result in deep SMTs and low AGHS. We also generalize the variation between AGHS and scaled SMT depth, a procedure that aids prediction of AGHS at different sites from observations of the SMT, such as along Cascadia Margin.

1. Introduction

Gas hydrates can form in the pore space of sediment along continental margins when methane and other low molecular weight gases combine with water at appropriate pressure, temperature and salinity conditions [Kvenvolden, 1993]. These hydrates are components of dynamic systems in which methane enters and leaves a gas hydrate stability zone (GHSZ) at variable rates [Dickens, 2003]. Based on the supply of methane, marine gas hydrate systems can be distinguished into two end-members: *in-situ* systems where microbes generate methane within the GHSZ [e.g., Claypool and Kvenvolden, 1983]; and deep-source systems where rising fluids bring methane from depth [e.g., Hyndman and Davis, 1992]. However, quantifying gas hydrate saturation in these systems remains a challenge. In this paper, we develop a model that relates average gas hydrate saturation (AGHS) to the depth of sulfate-methane transition (SMT) in deep-source systems. This facilitates prediction of AGHS at sites where SMT depth is known.

The SMT denotes a relatively thin zone near the seafloor where pore water sulfate and methane are depleted to zero concentration (Figure 1). This depletion occurs due to the anaerobic oxidation of methane reaction (AOM: $CH_4 + SO_4^{2-} \rightarrow HCO_3^- + HS^- + H_2O$) [Borowski *et al.*, 1999]. Although microbes can also consume sulfate using solid organic carbon [Bernier, 1980], AOM can dominate overall sulfate depletion in sediments with gas hydrates and

modest methane fluxes [Borowski et al., 1996; Snyder et al., 2007]. Further, since we focus only on deep-source gas hydrate systems (i.e., sites with low organic carbon input), AOM becomes the only sulfate sink. The sulfate profile and SMT depth in such deep-source systems should depend on methane flux from below because of the simple 1:1 AOM reaction [Borowski et al., 1996; Snyder et al., 2007]. Additionally, the thickness of the gas hydrate zone and gas hydrate saturation are functions of upward methane flux [Davie and Buffett, 2003; Bhatnagar et al., 2007]. Thus, SMT depth (L_s , Figure 1) should relate to gas hydrate saturation [Borowski et al., 1999].

To study this relationship between SMT depth and AGHS, we expand the model of Bhatnagar et al. [2007] by including a sulfate balance for deep-source systems (Figure 1). We show that, at steady-state conditions, the depth of the SMT relates to net fluid flux in the system and to AGHS (volume fraction of pore space) within the GHSZ. Compared to previous site-specific studies, our model generalizes the relationship between SMT depth and AGHS at any gas hydrate setting dominated by methane flux from depth.

2. Mathematical Model for Gas Hydrate Accumulation and AOM

Gas hydrate accumulation in marine sediment is simulated using a numerical model that includes phase equilibrium, sedimentation, diffusion, compaction-driven fluid flow, and external fluid flow [Bhatnagar et al., 2007]. Following Bhatnagar et al. [2007], the three-phase methane mass balance (liquid, gas hydrate and free gas) can be written to include the AOM reaction in dimensionless form as:

$$\begin{aligned} & \frac{\partial}{\partial \tilde{t}} \left[\frac{1+\gamma\tilde{\phi}}{\gamma} \left(S_w \tilde{c}_m^w + S_h \tilde{c}_m^h \tilde{\rho}_h + S_g \tilde{c}_m^g \tilde{\rho}_g \right) \right] + \\ & \frac{1+\gamma}{\gamma} \frac{\partial}{\partial \tilde{z}} \left[\left((Pe_1 + Pe_2) - Pe_1 \tilde{U}_s \frac{(1+\gamma\tilde{\phi})}{\gamma(1-\tilde{\phi})} S_h c_w^h \tilde{\rho}_h \right) \tilde{c}_m^w \right. \\ & \left. + Pe_1 \tilde{U}_s \frac{(1+\gamma\tilde{\phi})}{\gamma(1-\tilde{\phi})} \left(S_h \tilde{c}_m^h \tilde{\rho}_h + S_g \tilde{c}_m^g \tilde{\rho}_g \right) \right] = \quad (1) \\ & \frac{\partial}{\partial \tilde{z}} \left[\frac{1+\gamma\tilde{\phi}}{\gamma} S_w \frac{\partial \tilde{c}_m^w}{\partial \tilde{z}} \right] - Da_{AOM} \frac{M_{CH_4} c_{s,0}^w}{M_{SO_4} c_{m,eqb}^w} \left[\frac{1+\gamma\tilde{\phi}}{\gamma} S_w \right] \tilde{c}_m^w \tilde{c}_s^w \end{aligned}$$

where S_i represents saturation of phase i in pore space, $\tilde{\rho}_i$ is the density of phase i scaled by water density, M_j is molecular weight, and subscripts/superscripts w , h and g denote liquid water, hydrate and free gas phases, respectively. We normalize vertical depth as $\tilde{z} = z/L_t$, where L_t is depth to the base of GHSZ. Time is made dimensionless by a combination of L_t and methane diffusivity D_m ($\tilde{t} = t/(L_t^2/D_m)$).

Methane mass fraction in phase i (c_m^i) is scaled by methane solubility in the liquid phase at the base of GHSZ ($c_{m,eqb}^w$), c_w^h is mass fraction of water in hydrate phase ($c_w^h = 1 - c_m^h$), while sulfate mass fraction in pore water (c_s^w) is scaled by the seawater value ($c_{s,0}^w$), to get the corresponding normalized variables:

$$\tilde{c}_m^i = \frac{c_m^i}{c_{m,eqb}^w} \quad \text{for } i \in \{w, h, g\}, \quad \tilde{c}_s^w = \frac{c_s^w}{c_{s,0}^w} \quad (2)$$

Reduced porosity parameters, $\tilde{\phi}$ and γ , and normalized sediment flux, \tilde{U}_s , are defined as:

$$\tilde{\phi} = \frac{\phi - \phi_\infty}{1 - \phi_\infty}, \quad \gamma = \frac{1 - \phi_\infty}{\phi_\infty}, \quad \tilde{U}_s = \frac{U_s}{U_{f, sed}} \quad (3)$$

where ϕ is sediment porosity, ϕ_∞ is the minimum porosity at great depth, U_s is sediment flux, and $U_{f, sed}$ is the fluid flux resulting from sedimentation and compaction. Porosity loss is related to depth using a constitutive relationship between porosity and vertical effective stress assuming hydrostatic pressure [Bhatnagar et al., 2007]:

$$\tilde{\phi} = \frac{\eta}{\eta + (1 - \eta)e^{\tilde{z}}}, \quad \eta = \frac{\phi_0 - \phi_\infty}{1 - \phi_\infty} \quad (4)$$

where η and ϕ_0 are the reduced and actual porosities at the seafloor, respectively. $U_{f, sed}$ is related to seafloor sedimentation rate (\dot{S}) and porosities as follows [Berner, 1980]:

$$U_{f, sed} = \frac{1 - \phi_0}{1 - \phi_\infty} \dot{S} \phi_\infty \quad (5)$$

The two Peclet numbers Pe_1 , Pe_2 and the Damkohler number Da_{AOM} are defined as:

$$Pe_1 = \frac{U_{f, sed} L_t}{D_m}, \quad Pe_2 = \frac{U_{f, ext} L_t}{D_m}, \quad Da_{AOM} = \frac{\rho_w c_{m,eqb}^w \lambda_{AOM} L_t^2}{M_{CH_4} D_m} \quad (6)$$

where $U_{f, ext}$ is the upward fluid flux due to external sources and has negative value (due to opposite direction to $U_{f, sed}$), and λ_{AOM} is the second order rate constant for AOM. Thus, Pe_1 has positive value, while Pe_2 becomes negative. Since we focus on deep-source systems, results shown later are relevant for cases where $|Pe_2| > |Pe_1|$. Importantly, Pe_1 characterizes the ratio of compaction-driven fluid flux to methane diffusion, while Pe_2 represents the ratio of external

fluid flux to methane diffusion. The Damkohler number compares AOM rate to methane diffusion. Finally, we complete the system by formulating the dimensionless sulfate mass balance:

$$\begin{aligned} \frac{\partial}{\partial \tilde{t}} \left[\frac{1+\gamma\tilde{\phi}}{\gamma} S_w \tilde{c}_s^w \right] + \frac{1+\gamma}{\gamma} \frac{\partial}{\partial \tilde{z}} \left[\left((Pe_1 + Pe_2) - Pe_1 \tilde{U}_s \frac{(1+\gamma\tilde{\phi})}{\gamma(1-\tilde{\phi})} S_h c_w^h \tilde{\rho}_h \right) \tilde{c}_s^w \right] = \\ \frac{\partial}{\partial \tilde{z}} \left[\frac{1+\gamma\tilde{\phi}}{\gamma} S_w \left(\frac{D_s}{D_m} \right) \frac{\partial \tilde{c}_s^w}{\partial \tilde{z}} \right] - Da_{AOM} \left[\frac{1+\gamma\tilde{\phi}}{\gamma} S_w \right] \tilde{c}_m^w \tilde{c}_s^w \end{aligned} \quad (7)$$

where D_s denotes sulfate diffusivity. The initial and boundary conditions for the two mass balances are written as:

$$\text{I.C.: } \tilde{c}_s^w(\tilde{z}, 0) = \tilde{c}_m^w(\tilde{z}, 0) = 0 \quad (8)$$

$$\text{B.C. (1): } \tilde{c}_s^w(0, \tilde{t}) = 1 \quad , \quad \tilde{c}_m^w(0, \tilde{t}) = 0 \quad (9)$$

$$\text{B.C. (2): } \frac{\partial \tilde{c}_s^w}{\partial \tilde{z}}(D, \tilde{t}) = 0 \quad , \quad \tilde{c}_m^w(D, \tilde{t}) = \tilde{c}_{m,ext}^w = \frac{c_{m,ext}^w}{c_{m,eqb}^w} \quad (10)$$

where $c_{m,ext}^w$ is the methane concentration in the external flux, $\tilde{c}_{m,ext}^w$ is the normalized value, and D denotes the bottom of the model domain.

3. Results

Equations (1) and (7) are solved numerically to obtain steady-state profiles for methane, gas hydrate saturation, and pore water sulfate concentration. For results shown later, we assume seafloor temperature (T_0) to be 3°C, geothermal gradient (G) to be 0.04°C/m, and pore water salinity representative of standard seawater. Changing T_0 or G results in methane solubility curves that are similar in the normalized form [Bhatnagar *et al.*, 2007], causing AGHS to be relatively insensitive to changes in T_0 or G . However, the normalized solubility curves are more sensitive to seafloor depth. Thus, we use a seafloor depth of 1000 m for results shown in Figures 2 and 3, whereas Figure 4 generalizes the relationship between AGHS and SMT depth for multiple seafloor depths. Porosity at the seafloor (ϕ_0) and at depth (ϕ_∞) are assumed to be 0.7 and 0.1, respectively. Diffusivities D_s and D_m are taken to be 0.56×10^{-9} and 0.87×10^{-9} m²/s, respectively [Iversen and Jørgensen, 1993], c_m^h is set to 0.134, seawater sulfate concentration equals 28 mM, and ρ_h and ρ_f equal 930 and 1030 kg/m³, respectively. At steady state, $\tilde{c}_{m,ext}^w$ is not significant, provided it exceeds the minimum required to form hydrate [Bhatnagar *et al.*, 2007]. Consequently, we assume in all simulations here that $\tilde{c}_{m,ext}^w$ equals unity.

We first study the effect of Da_{AOM} on steady-state profiles. For fixed Pe_1 and Pe_2 , decreasing Da_{AOM} results in a thickening of the SMT zone (Figure 2a). Higher Da_{AOM} implies faster consumption of methane and sulfate compared to diffusion, causing a relatively sharp SMT. The thickness of the SMT zone is usually less than a few meters at most gas hydrate settings, so we use a large value of Da_{AOM} (10^8) in further simulations.

Concentration profiles simulated for three different sets of Pe_1 and Pe_2 , but with the sum $Pe_1 + Pe_2$ held constant at -10, are shown in Figure 2b. Overlap of these profiles demonstrates that neither Pe_1 nor Pe_2 individually controls the concentration profiles, but that their sum determines the concentrations and the scaled SMT depth, $\tilde{L}_s = L_s / L_t$. This sum, $Pe_1 + Pe_2$, represents the net fluid flux through the system. Hydrate saturation profiles, however, depend on more than the sum of the Peclet numbers (Figure 2c). The AGHS ($\langle S_h \rangle$) for each of the three cases is about 0.2%, 0.5% and 2%, with the highest value corresponding to the smallest Pe_1 (0.1) and largest Pe_2 (-10.1). Small Pe_1 and large Pe_2 correspond to low sedimentation rate and high methane flux, respectively, resulting in higher AGHS. However, for all three cases, the product $Pe_1 \langle S_h \rangle$ is the same. Thus, Figure 2c demonstrates that $Pe_1 \langle S_h \rangle$, which characterizes the flux of gas hydrate through the GHSZ, is controlled by the net fluid flux, $Pe_1 + Pe_2$ [Bhatnagar et al., 2007].

Increasing net methane flux from depth (i.e., raising the magnitude of $Pe_1 + Pe_2$) results in a shallow scaled SMT depth (Figure 3a), as proposed by Borowski et al. [1996, 1999]. Increasing Pe_2 , with Pe_1 held constant, increases gas hydrate saturation (Figure 3b) due to higher methane input to the system. Consequently, $Pe_1 \langle S_h \rangle$ also increases. Hence, the scaled depth to the SMT, \tilde{L}_s , and $Pe_1 \langle S_h \rangle$ both depend on the sum $Pe_1 + Pe_2$. As a consequence, scaled SMT depth and $Pe_1 \langle S_h \rangle$ become correlated. This correlation, shown in Figure 4 for three seafloor depths, indicates that average gas hydrate flux, $Pe_1 \langle S_h \rangle$, increases as \tilde{L}_s decreases. Thus, AGHS can be estimated for any system dominated by methane flux from depth if \tilde{L}_s and Pe_1 are known (Figure 4).

4. Application to Cascadia Margin Sites

Sites drilled by Ocean Drilling Program (ODP) Leg 146 and Integrated Ocean Drilling Program Expedition (IODP) 311 penetrate gas hydrate accumulations along Cascadia Margin [Westbrook et al., 1994; Riedel et al., 2006]. The low organic carbon content of sediment and pervasive upward fluid migration at these sites suggests that gas hydrate in the Cascadia Margin is

controlled by methane supplied from depth [Riedel *et al.*, 2006]. We now summarize calculation of AGHS from site-specific data at Cascadia Margin Sites 889, U1325, U1326 and U1328 (Table 1):

- Use sedimentation rate (\dot{S}) to calculate Pe_1 from equations (5) and (6);
- Calculate the scaled SMT depth \tilde{L}_s using the dimensional depths L_s and L_t ;
- For given seafloor depth and \tilde{L}_s , obtain gas hydrate flux $Pe_1 \langle S_h \rangle$ from Figure 4;
- Divide this gas hydrate flux by Pe_1 to yield AGHS, $\langle S_h \rangle$ (Table 1)

At Site 889 (ODP Leg 146), pore water chloride profile indicates a peak hydrate saturation close to 2% at the base of GHSZ, and AGHS <1% within the GHSZ [Davie and Buffett, 2003]. This result agrees favorably with our simulation that shows peak saturation of about 2.2 % at the base of GHSZ and AGHS of 0.4% across the entire GHSZ (Table 1). Hyndman *et al.* [1999] calculated gas hydrate saturation between 25-30% of pore space in the 100 m interval above the base of GHSZ at Site 889 using resistivity log data. Subsequent calculations using a different set of Archie parameters revise this estimate to 5-10% in that 100 m interval [Riedel *et al.*, 2006]. Further, Ussler and Paull [2001] show that a smoothly decreasing chlorinity profile at Site 889 yields hydrate saturation of 2-5% within discrete layers. Although several parameter uncertainties confront such estimates [Egeberg and Dickens, 1999; Riedel *et al.*, 2006], AGHS predicted using our SMT model concurs with the lower estimates at Site 889.

For the IODP Expedition 311 sites, drilled along the northern Cascadia Margin, we compare our predictions with AGHS computed from chloride anomalies and resistivity log data (Table 1). AGHS is calculated from chloride data by assuming a background *in situ* chloride profile and attributing the relative pore water freshening to gas hydrate dissociation [e.g., Egeberg and Dickens, 1999]. AGHS is obtained from resistivity data using the Archie equation and parameters given in Riedel *et al.* [2006]. AGHS at Sites U1325 and U1326 estimated from resistivity and chlorinity are similar and our predictions based on SMT depth are close to these estimates (Table 1). At Site U1328, our predicted AGHS is distinctly lower than resistivity-based estimate (Table 1). Site U1328 is a cold vent characterized by focused fluid and gas flow that causes high gas hydrate saturations close to the seafloor [Riedel *et al.*, 2006]. Such local heterogeneities that might enhance methane flux from depth are not included in our simple 1-D model, thereby causing greater deviation between predicted and estimated AGHS.

Overall, we get good first order agreement between AGHS derived from chloride anomalies/resistivity logs and those predicted using our model, although our simulations consistently show lower AGHS at these sites. A possible explanation for this general deviation is that interpretations of resistivity logs

depend on knowledge of formation water resistivity and three empirical constants, which are hard to constrain in clay-rich sediments. Additionally, our simulations (Figures 2 and 3) and previous models [e.g., *Davie and Buffett, 2003*] predict gas hydrate to first occur well below the seafloor. In contrast, log-based results often predict hydrate starting immediately below the seafloor, causing AGHS to be higher than that predicted from simple transport models. Apart from the small deviations between model and chloride/resistivity log predictions, our model captures the trend in the lateral variation of AGHS correctly and likely provides a lower bound on AGHS. Hence, our model and generalized results (Figure 4) provide a simple and fast technique to constrain AGHS in deep-source gas hydrate systems.

5. Conclusions

We show that scaled depth to the SMT (\tilde{L}_s) can be used to estimate AGHS for deep-source gas hydrate systems. Simulation results demonstrate that the net fluid flux controls \tilde{L}_s and the average gas hydrate flux ($Pe_1 \langle S_h \rangle$) through the GHSZ, thereby allowing us to correlate \tilde{L}_s and $Pe_1 \langle S_h \rangle$. Results also show that conditions that create shallow \tilde{L}_s and low Peclet number (Pe_1) lead to higher AGHS. Application of this method to sites along Cascadia Margin reveals a good match with saturations estimated from chloride/resistivity log data and accurately predicts the lateral variability in AGHS.

Acknowledgments. We acknowledge financial support from the Shell Center for Sustainability, the Kobayashi Graduate Fellowship, and the Department of Energy (DE-FC26-06NT42960). We thank Janice Hewitt for help with editing this manuscript. Comments from anonymous reviewers improved this manuscript.

References

- Berner, R. A. (1980), *Early Diagenesis : A Theoretical Approach*, Princeton Univ. Press, Princeton, N.J.
- Bhatnagar, G., W. G. Chapman, G. R. Dickens, B. Dugan, and G. J. Hirasaki (2007), Generalization of gas hydrate distribution and saturation in marine sediments by scaling of thermodynamic and transport processes, *Am. J. Sci.*, 307, 861-900.
- Borowski, W. S., C. K. Paull, and W. Ussler III (1996), Marine pore-water sulfate profiles indicate in situ methane flux from underlying gas hydrate, *Geology*, 24(7), 655-658.
- Borowski, W. S., C. K. Paull, and W. Ussler III (1999), Global and local variations of interstitial sulfate gradients in deep-water, continental margin sediments: Sensitivity to underlying methane and gas hydrates, *Mar. Geol.*, 159, 131-154.

- Claypool, G. E., and K. A. Kvenvolden (1983), Methane and other hydrocarbon gases in marine sediment, *Annu. Rev. Earth Planet. Sci.*, 11, 299-327.
- Davie, M. K., and B. A. Buffett (2003), Sources of methane for marine gas hydrate: inferences from a comparison of observations and numerical models, *Earth Planet. Sci. Lett.*, 206, 51-63.
- Dickens, G. R. (2003), Rethinking the global carbon cycle with a large, dynamic and microbially mediated gas hydrate capacitor, *Earth Planet. Sci. Lett.*, 213, 169-183.
- Hyndman, R. D., and E. E. Davis (1992), A mechanism for the formation of methane hydrate and seafloor bottom-simulating reflectors by vertical fluid expulsion, *J. Geophys. Res. B*, 97, 7025-7041.
- Hyndman, R. D., T. Yuan, and K. Moran (1999), The concentration of deep sea gas hydrates from downhole electrical resistivity logs and laboratory data, *Earth Planet. Sci. Lett.*, 172, 167-177.
- Iversen, N., and B. B. Jørgensen (1993), Diffusion coefficients of sulfate and methane in marine sediments: Influence of porosity, *Geochim. Cosmochim. Acta*, 57, 571-578.
- Kvenvolden, K. A. (1993), Gas hydrates: Geological perspective and global change, *Rev. Geophys.*, 31, 173-187.
- Riedel, M., T. S. Collett, M. J. Malone, and the Expedition 311 Scientists (Eds.) (2006), *Proc. IODP*, vol. 311, Integrated Ocean Drilling Program Management International Inc., Washington, DC.
- Snyder, G. T., A. Hiruta, R. Matsumoto, G. R. Dickens, H. Tomaru, R. Takeuchi, J. Komatsubara, Y. Ishida, and H. Yu (2007), Pore water profiles and authigenic mineralization in shallow marine sediments above the methane-charged system on Umitaka Spur, Japan Sea, *Deep-Sea Res. II*, 54, 1216-1239.
- Ussler, W., and C. K. Paull (2001), Ion exclusion associated with marine gas hydrate deposits, in *Natural Gas Hydrates: Occurrence, Distribution, and Detection*, *Geophys. Monogr. Ser.*, vol. 124, edited by C. K. Paull and W. P. Dillon, pp. 41-51, AGU, Washington, D. C.
- Westbrook, G. K., B. Carson, and R. J. Musgrave et al. (Eds.) (1994), *Proc. ODP, Initial Reports*, vol. 146 (Pt. 1), Ocean Drilling Program, College Station, TX.

Table 1. Site-specific parameters and calculated AGHS for Cascadia Margin sites compared with estimates from resistivity log data and chloride anomalies

Site	\dot{S} (cm/k.y.)	Pe_1	Seafloor depth (m)	L_s/L_t (m/m) = \tilde{L}_s	$Pe_1 \langle S_h \rangle$ (Figure 4)	$\langle S_h \rangle$ (calc.)	$\langle S_h \rangle$ (res. log)	$\langle S_h \rangle$ (Cl ⁻)
889 ^a	25	0.07	1311	10/225 = 0.044	0.03	0.4%	-	<1% ^b
U1325 ^c	38.3	0.11	2195	4.5/230 = 0.02	0.22	2%	3.7% ^e	5.3% ^f
U1326 ^c	38.3 ^g	0.11	1828	2.5/230 = 0.011	0.46	4.2%	6.7% ^e	5.5% ^f
U1328 ^c	34.3	0.09	1267	1.5/219 = 0.007	0.67	7.4%	12.6% ^e	-

^a ODP Leg 146 [*Westbrook et al.*, 1994]

^b Taken from numerical model of *Davie and Buffett*, 2003

^c IODP Expedition 311 [*Riedel et al.*, 2006]

^e Calculated from Archie equation using resistivity log data [*Riedel et al.*, 2006]

^f Calculated using relative freshening of pore water chloride profiles [*Riedel et al.*, 2006]

^g \dot{S} was not available, hence assumed equal to rate at nearest site U1325

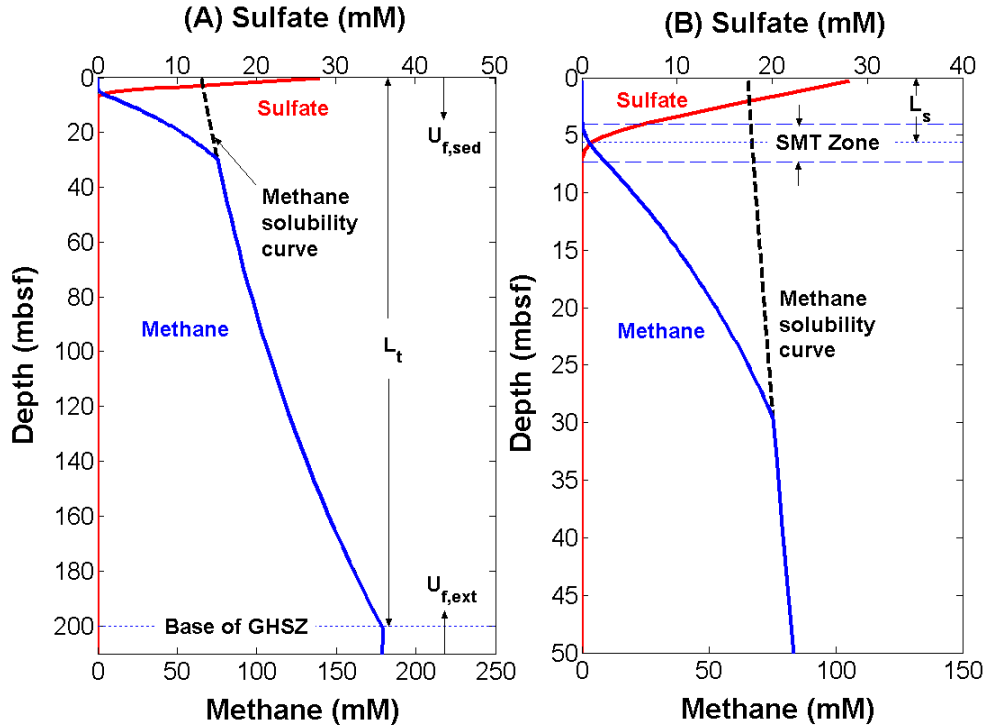


Figure 1. (A) Schematic representation of a gas hydrate system showing pore water sulfate and methane concentrations, which go to zero at some shallow depth because of anaerobic oxidation of methane (AOM). Also shown are methane solubility in water, the two fluid fluxes ($U_{f, sed}$ and $U_{f, ext}$), and depth to the base of the gas hydrate stability zone (L_t). (B) Close-up of the sulfate-methane transition (SMT) showing overlap of sulfate and methane profiles, and its depth below the seafloor (L_s).

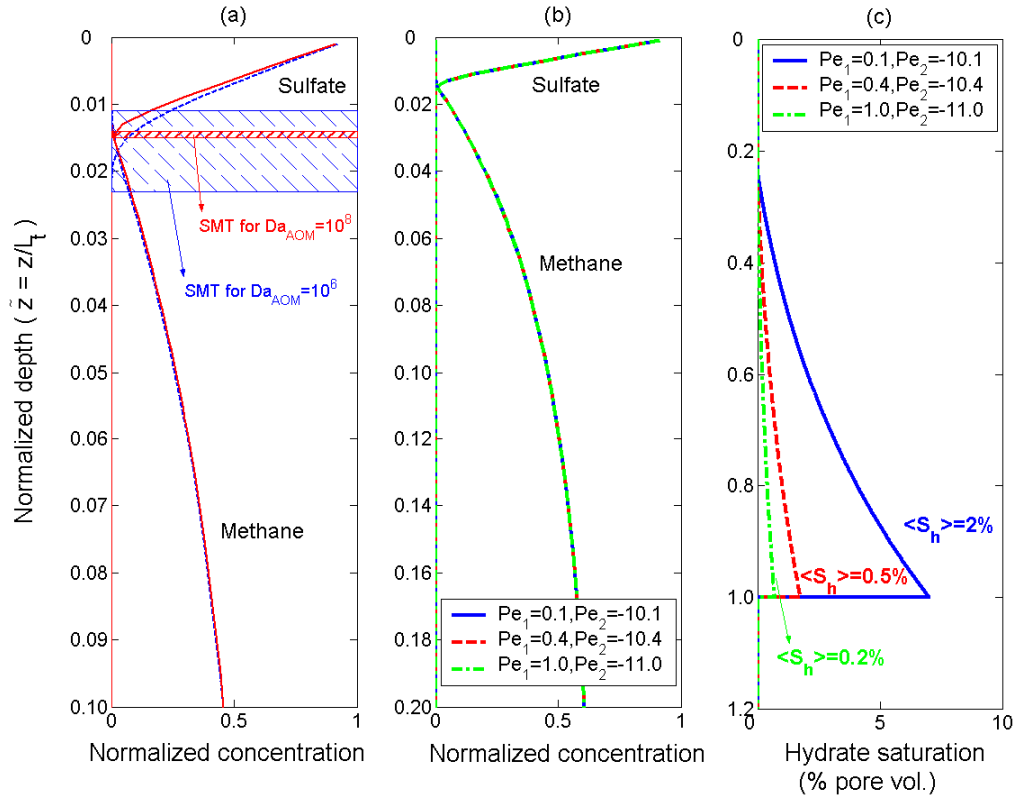


Figure 2. Effect of Damkohler number (Da_{AOM}) and Peclet numbers (Pe_1, Pe_2) on steady-state profiles. $Pe_1 + Pe_2 = -10$ for all cases. Note different y-axis scale for each plot. (a) Sulfate and methane profiles for $Da_{AOM} = 10^8$ (solid curves) and $Da_{AOM} = 10^6$ (dashed curves). Hatched regions compare the thickness of the SMT for the two cases. (b) Simulations for different sets of Pe_1 and Pe_2 , with $Pe_1 + Pe_2 = -10$. Overlap of methane and sulfate profiles shows that $Pe_1 + Pe_2$ controls the concentrations. (c) The product $Pe_1 \langle S_h \rangle$ depends on $Pe_1 + Pe_2$, but hydrate saturation profiles are a function of Pe_1 .

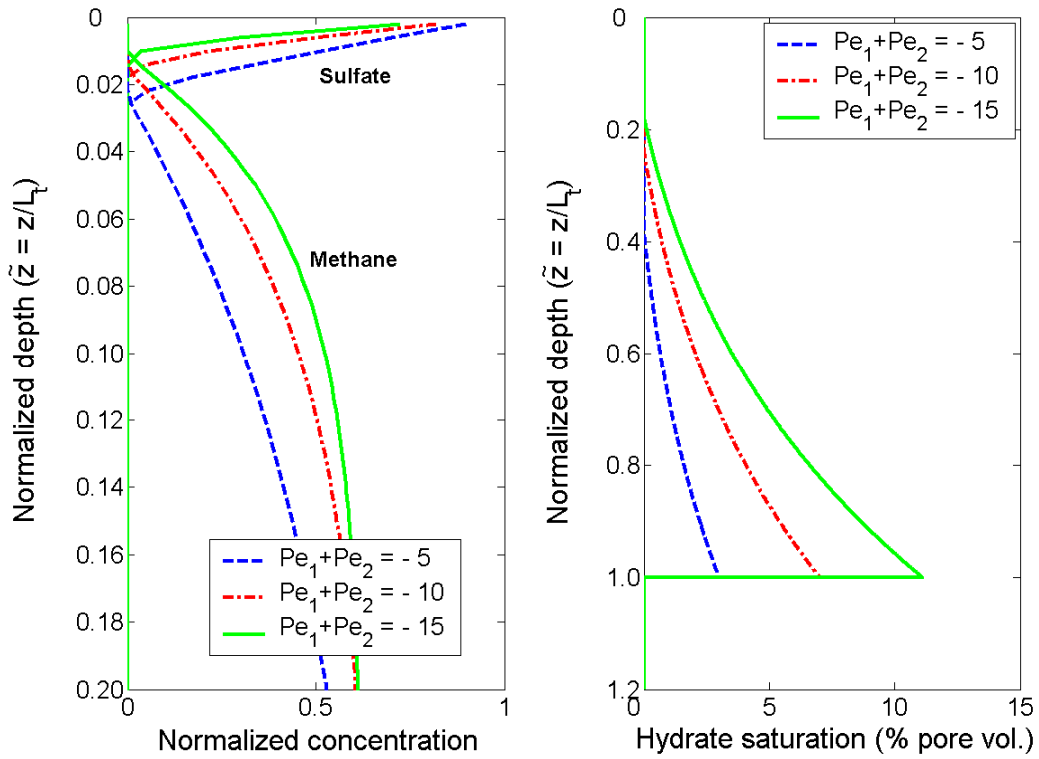


Figure 3. Effect of net fluid flux ($Pe_1 + Pe_2$) on steady-state concentrations. Pe_1 equals 0.1 for all simulations. (a) High magnitude of $Pe_1 + Pe_2$ defines higher net methane fluxes, resulting in shallower SMT zones. (b) Gas hydrate saturation at steady state increases as magnitude of $Pe_1 + Pe_2$ increases.

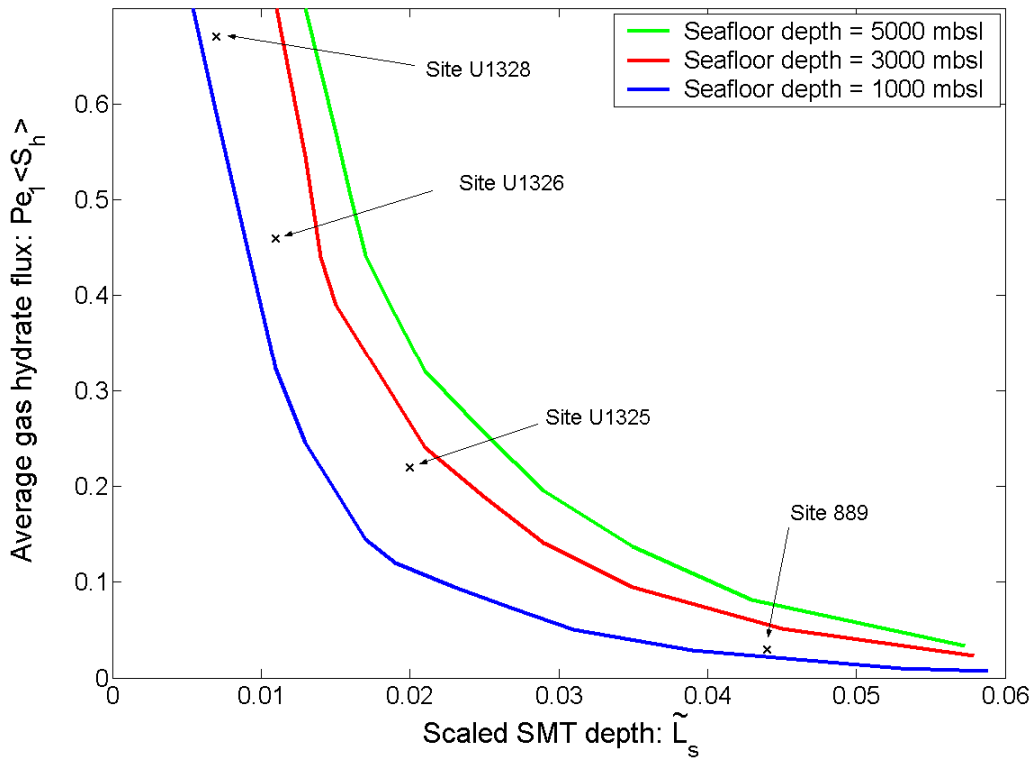


Figure 4. Relationship between average gas hydrate flux $Pe_1 \langle S_h \rangle$ and scaled SMT depth ($\tilde{L}_s = L_s / L_t$) for several seafloor depths. Points corresponding to four Cascadia Margin sites are plotted to show how AGHS is estimated from \tilde{L}_s using this plot (Table 1).